Efficient Concomitant and Remanence Field Artifact Reduction in Ultra-Low-Field MRI Using a Frequency-Space Formulation

Yi-Cheng Hsu,[1,2] Panu T. Vesanen,[2] Jaakko O. Nieminen,[2] Koos C.J. Zevenhoven,[2] Juhani Dabek,[2] Lauri Parkkonen,[2] I-Liang Chern,[1] Risto J. Ilmoniemi,[2] and Fa-Hsuan Lin[2,3]*

Purpose: For ultra-low-field MRI, the spatial-encoding magnetic fields generated by gradient coils can have strong concomitant fields leading to prominent image distortion. Additionally, using superconducting magnet to pre-polarize magnetization can improve the signal-to-noise ratio of ultra-low-field MRI. Yet the spatially inhomogeneous remanence field due to the permanently trapped flux inside a superconducting pre-polarizing coil modulates magnetization and causes further image distortion.

Method: We propose a two-stage frequency–space (*f–x*) formulation to accurately describe the dynamics of spatially-encoded magnetization under the influence of concomitant and remanence fields, which allows for correcting image distortion due to concomitant and remanence fields.

Results: Our method is computationally efficient as it uses a combination of the fast Fourier transform algorithm and a linear equation solver. With sufficiently dense discretization in solving the linear equation, the performance of this *f–x* method was found to be stable among different choices of the regularization parameter and the regularization matrix.

Conclusion: We present this method together with numerical simulations and experimental data to demonstrate how concomitant and remanence field artifacts in ultra-low-field MRI can be corrected efficiently. **Magn Reson Med 71:955–965, 2014. © 2013 Wiley Periodicals, Inc.**

Key words: low field; distortion; concomitant field; remanence field; time domain reconstruction

INTRODUCTION

In contrast to high-field MRI, ultra-low-field (ULF) MRI uses a magnetic field in the microtesla range for magnetization precession (1). To increase the signal-to-noise ratio (SNR), the pre-polarization technique (2) has been used to magnetize first the sample in a stronger millitesla-range field and then to allow magnetization precession in the microtesla range for signal detection. In addition, superconducting quantum interference devices (SQUIDs) have been used to detect the weak precessing magnetization (for review, see Ref. 1)). Acquiring MRI in the microtesla range gives ULF MRI several advantages: acoustically silent acquisition, low projectile danger and thus safe operation, imaging compatibility with metal objects, and an MRI system with open access. In addition, it has been suggested that the T_1 contrast in healthy (3) and malignant (4) tissues is higher in low magnetic fields than in the tesla range. Finally, it has been demonstrated that magnetoencephalography can be combined with ULF MRI in a single hybrid system (4,5).

A technical challenge of ULF MRI is the concomitant-field effect (4,6–8), which is typically ignored in high-field MRI except in some special cases (such as phase-contrast MR (9), echo planar imaging (10,11), spiral scan (12), balanced steady-state free precession (13), and fast spin echo imaging (14)). According to Maxwell's equations, the curl and divergence of a source-free static magnetic field are zero. Thus, a uniform magnetic field gradient in one direction must be accompanied with at least one other magnetic field gradient in a different direction. In high-field MRI with a strong B_0, this concomitant field is usually neglected, because B_0 is much stronger than the concomitant field. However, in ULF MRI, B_0 is often of the same order of magnitude as the maximum of the gradient fields used for spatial encoding. Thus, artifacts, including blurring and distortion, appear if image reconstruction only takes linear gradients into consideration.

Concomitant field artifacts can be reduced by using customized MRI hardware or pulse sequences (15–18). However, it can be more convenient to use image reconstruction algorithms to correct for these artifacts. For example, when the concomitant field is large only along the frequency encoding direction, the distortion artifacts can be corrected by providing the image reconstruction the correct local precession frequencies (19). When the concomitant field is non-negligible in both frequency and phase encoding directions, the associated blurring and distortion artifacts can be reduced after carefully calibrating the local magnetization phase and the corresponding precession frequency (20). However, both image processing methods cannot reduce the concomitant field artifacts satisfactorily when the concomitant

[1]Department of Mathematics, National Taiwan University, Taipei, Taiwan.

[2]Department of Biomedical Engineering and Computational Science, Aalto University School of Science, Espoo, Finland.

[3]Institute of Biomedical Engineering, National Taiwan University, Taipei, Taiwan.

Grant sponsor: National Science Council, Taiwan (NSC); Grant number: 100–2917-I-564-027; Grant sponsor: National Science Council, Taiwan (NSC); Grant number: 101–2628-B-002–005-MY3; Grant sponsor: Ministry of Economic Affairs, Taiwan; Grant number: 100-EC-17-A-19-S1–175; Grant sponsor: National Health Research Institute, Taiwan; Grant number: NHRI-EX102–10247EI; Grant sponsor: Academy of Finland (the FiDiPro program) and the European Community's Seventh Framework Programme (FP7/2007–2013); Grant number: 200859.

*Correspondence to: Fa-Hsuan Lin, Ph.D., Institute of Biomedical Engineering, National Taiwan University, 1, Sec. 4, Roosevelt Road, Taipei, 106, Taiwan. E-mail: fhlin@ntu.edu.tw

Received 17 August 2012; revised 28 February 2013; accepted 8 March 2013

DOI 10.1002/mrm.24745

Published online 13 May 2013 in Wiley Online Library (wileyonlinelibrary.com).

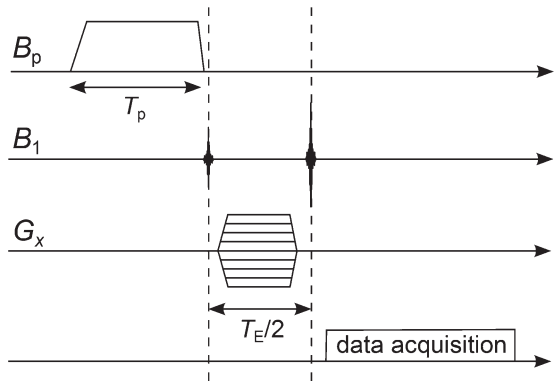

FIG. 1. The spin-echo pulse sequence used in the simulation and experiments. The B_0 field and the frequency-encoding gradient were constantly on. The polarizing time T_p was 3 s and the echo time T_E was 121 ms.

field is strong (relative to B_0) because the irregular phase encoding causes the encoded phase variation rate spread into a wide bandwidth. One way to reconstruct images using measurements under a strong concomitant field is to carefully describe the relationship between the received signal and magnetization dynamics over space using linear equations (21). However, without further simplification, the encoding matrix of such an approach is often too large to be inverted practically.

To compensate for the low native SNR of ULF MRI, a separate strong polarization field has been used to boost the magnetization (1). Recently, it has been demonstrated that a superconducting magnet can be used to generate a pre-polarizing field (5). Benefits of a superconducting magnet are, e.g., its compact size and zero resistance leading to negligible heat generation (5). However, the use of a superconducting pre-polarization magnet also causes artifacts due to a remanence field, which is the magnetic field generated by permanently trapped flux inside the superconducting pre-polarizing coil. Thus, even after turning off the pre-polarizing magnet, the spatially inhomogeneous remanence field still exists and modulates the magnetization dynamics. To our knowledge, correction of this kind of a distortion has so far not been addressed in the ULF MRI image reconstruction.

A potential advantage of ULF MRI is to produce quantitative measurements. For example, susceptibility, conductivity-, and permittivity-related artifacts are greatly reduced in the ULF range. However, to take advantage of these quantitative measurements in practice, image distortion arising from the concomitant and remanence fields must be corrected. Furthermore, ULF MRI holds the promise of measuring magnetoencephalography and MRI using the same device and thereby improving coregistration between magnetoencephalography and MRI (22). However, this also requires distortion-free ULF MRI.

Here, we propose a two-stage frequency-encoding real-space (f–x) formulation to accurately describe the dynamics of the spatially-encoded magnetization. Reconstructing images using data described by the f–x formulation can correct distortion due to concomitant and remanence fields, because these disturbances are incorporated in the formulation explicitly. Compared with the full time-domain reconstruction (TDR) (21), the complexity of this f–x formulation is lower. We present this method together with numerical simulations and experimental data to demonstrate how concomitant and remanence field artifacts in ULF MRI can be corrected efficiently.

THEORY

In our ULF-MRI setup, the total magnetic field $\mathbf{b}(\mathbf{r})$ experienced by the magnetization is

$$\mathbf{b}(\mathbf{r}) = \mathbf{b}_{\text{ideal}}(\mathbf{r}) + \mathbf{b}_{\text{con}}(\mathbf{r}) + \mathbf{b}_{\text{rem}}(\mathbf{r}), \quad [1]$$

with the ideal magnetic field

$$\mathbf{b}_{\text{ideal}}(\mathbf{r}) = (B_0 + \mathbf{g}^{\text{T}}\mathbf{r})\mathbf{e}_z, \quad [2]$$

where B_0 is the main field and $\mathbf{g} = [g_x\ g_y\ g_z]^{\text{T}}$ is the ideal linear magnetic field gradient for spatial encoding. The concomitant field is approximately

$$\mathbf{b}_{\text{con}}(\mathbf{r}) = (-g_z x/2 + g_x z)\mathbf{e}_x + (-g_z y/2 + g_y z)\mathbf{e}_y, \quad [3]$$

where $\mathbf{e}_x$, $\mathbf{e}_y$, and $\mathbf{e}_z$ are orthogonal unit vectors in the Cartesian coordinate system. $\mathbf{b}_{\text{rem}}(\mathbf{r})$ denotes the spatial distribution of the remanence field. The strength of the concomitant-field effects depends on the ratio between $|\mathbf{b}_{\text{ideal}}(\mathbf{r})|$ and $|\mathbf{b}_{\text{con}}(\mathbf{r})|$. Therefore, $\varepsilon = (g^{\max} \times \text{FOV})/B_0$ is used to quantify the effect of the concomitant field (20,21), where $g^{\max}$ is the maximal gradient strength used during the pulse sequence and FOV is the side length of a square centered at the origin, where $\mathbf{b}_{\text{con}}(\mathbf{r}) = 0$, which enclose the field of view (FOV). Typically, ULF MRI has $0.1 < \varepsilon < 1$ (19,20).

To better understand how concomitant field can lead to image distortion, we consider the magnetization at location (0, y, z) in a two-dimensional spin-echo pulse sequence (Fig. 1). We first discuss the precession of magnetization in frequency encoding. The magnetization will experience the magnetic field

$$\begin{aligned} B_x &= 0 \\ B_y &= -g_z y/2 \\ B_z &= B_0 + g_z z \end{aligned}$$

and precess at frequency

$$\omega = \gamma\sqrt{(B_0 + g_z z)^2 + (g_z y/2)^2}, \quad [4]$$

higher than the ideal situation, where the concomitant field is neglected ($g_z y = 0$). Such a deviation from the resonance frequency $\gamma(B_0 + g_z z)$ will cause mis-localization of the magnetization since its physical precession frequency is higher.

Then we consider the phase encoding process. During the ith phase encoding step ($1 \le i \le N_{\text{ph}}$), the magnetization at location (0, y, z) experiences a magnetic field:

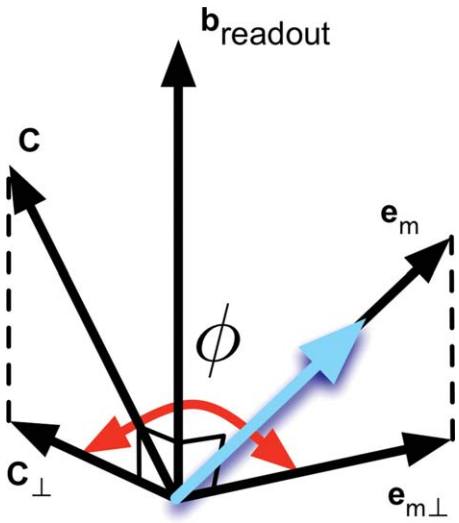

FIG. 2. Directions of the magnetization at the beginning of the read-out, the total magnetic field during the read-out, and the field sensitivity of a pick-up coil.

$$\begin{aligned} B_x &= 0 \\ B_y &= -g_z y/2 + g_y{}^{\max} z \times \left(i - N_{\mathrm{ph}}/2 - 1\right)/(N/2) \\ B_z &= B_0 + g_z z + g_y{}^{\max} y \times \left(i - N_{\mathrm{ph}}/2 - 1\right)/\left(N_{\mathrm{ph}}/2\right), \end{aligned} \quad [5]$$

which indicate that (1) most of the time, the precession axis is different from the precession axis of frequency encoding, (2) the precession axis varies at different phase encoding steps, and (3) the precession frequency between adjacent phase-encoding does not increase at constant rate. These effect will together cause image blurring if Fourier transform is directly used for image reconstruction.

Given the spatial distribution of the total magnetic field, we attempt to describe accurately the dynamics of magnetization precession during the read-out of an N-step phase-encoded ULF-MRI experiment ($1 \le n \le N$). We first define a unit vector $\mathbf{e}_{\mathrm{m}}(\mathbf{r}, n)$ as the direction of the magnetization $\mathbf{m}(\mathbf{r},n) = \rho(\mathbf{r})\mathbf{e}_{\mathrm{m}}(\mathbf{r}, n)$ at the beginning of the read-out after the nth phase encoding step, where $\rho(\mathbf{r})$ denotes the net polarized spin density at location $\mathbf{r}$. Furthermore, let $\mathbf{c}(\mathbf{r})$ denotes the vector of the B_1 field sensitivity of a pick-up coil at location $\mathbf{r}$. The detected AC signal $s(t,n)$ at a time t after the nth phase encoding is

$$s(t,n) = \int_V \rho(\mathbf{r})|\mathbf{e}_{\mathrm{m}\perp}(\mathbf{r},n)|\cos\left(\gamma|\mathbf{b}_{\mathrm{readout}}(\mathbf{r})|t + \phi(\mathbf{r},n)\right)|\mathbf{c}_{\perp}(\mathbf{r})|d\mathbf{r}, \quad [6]$$

where $|\mathbf{e}_{\mathrm{m}\perp}(\mathbf{r}, n)|$ and $|\mathbf{c}_{\perp}(\mathbf{r})|$ are the magnitudes of $\mathbf{e}_{\mathrm{m}}(\mathbf{r}, n)$ and $\mathbf{c}(\mathbf{r})$ perpendicular to the total magnetic field during readout $\mathbf{b}_{\mathrm{readout}}(\mathbf{r})$, which includes the ideal spatial encoding field, concomitant field, and the remanence field. γ is the gyromagnetic ratio and $\phi(\mathbf{r},n)$ is the accrued phase from the perpendicular component of the magnetization $\mathbf{e}_{\mathrm{m}\perp}(\mathbf{r}, n)$ by the end of the phase encoding step n and the perpendicular component of the coil sensitivity $\mathbf{c}_{\perp}(\mathbf{r})$. Note that because of concomitant fields, the magnetization precession axis in phase encoding is *not* in parallel with the magnetization precession axis in frequency encoding. Consequently the evolution of the phase of magnetization becomes complicated in phase encoding and frequency encoding. In other words, although $\phi(\mathbf{r},n)$ is a phase of the magnetization, it is different from the definition of the phase in high-field MRI during phase encoding. Figure 2 shows these vectors.

Given $|\mathbf{b}_{\mathrm{readout}}(\mathbf{r})|$, we can generate a map of iso-frequencies, each one of which delineates a curvilinear surface (lines in two-dimensional imaging) of magnetizations precessing at identical frequencies (Fig. 3, upper left panel). The maximum, minimum, and the spacing of these iso-frequency curves depends on the upper/lower bounds of the $|\mathbf{b}_{\mathrm{readout}}(\mathbf{r})|$ within the FOV and the duration of the data acquisition.

For simplicity, we consider MRI measurements consisting of steps of phase-encoded readouts. Thus, our formulation can be applied to either two-dimensional or three-dimensional imaging. Provided with (i) a map of total magnetic field strength during readout, and (ii) a vector map of total magnetic field during each phase encoding step, the *f–x* formulation consists of two stages: first, at each phase-encoding step, we apply fast Fourier transform to $s(t,n)$ to estimate amplitude and phases of each discretized frequency (the "*f*" step). At each discretized frequency, this complex-valued signal is the integral of the unknown magnetization distribution

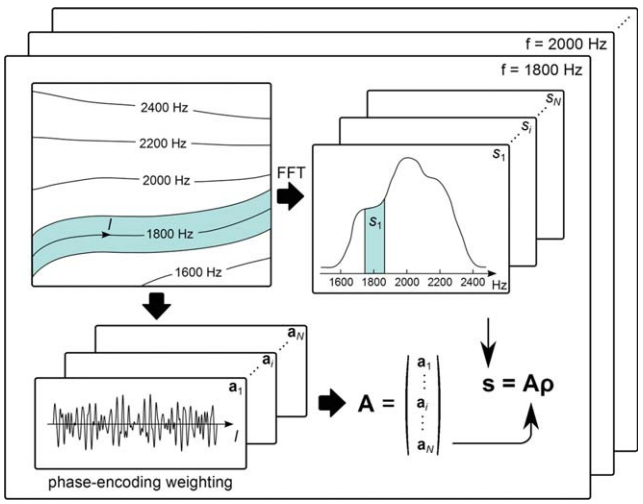

FIG. 3. Flowchart of the *f–x* reconstruction method. In upper left panel, the map of the iso-frequency curves during the signal read-out. In lower left panel, the phase-encoding weightings $|\mathbf{e}_{\mathrm{m}\perp}(\mathbf{r},n)|\exp\left(j\phi(\mathbf{r},n)\right)|\mathbf{c}_{\perp}(\mathbf{r})|J(\mathbf{r})$ along the chosen iso-frequency curve (1800 Hz). These weightings across the phase-encodings can be combined to form a matrix **A**. In upper right panel, the FFT of the signal during read-out after the various phase encodings. The complex signals at the chosen frequency (1800 Hz) across the phase-encodings can be used to form a signal vector **s**. The matrix **A** and the signal s are related by $\mathbf{s} = \mathbf{A}\boldsymbol{\rho}$, where $\boldsymbol{\rho}$ is the vector of spin-densities along the chosen iso-frequency curve. This procedure is repeated to cycle through all the iso-frequency curves.

(precessing at the same frequency) along an iso-frequency curve weighted by a spatial function determined by the total magnetic field during the phase encoding step (Fig. 3, upper right panel). Second, at each discretized frequency, complex-valued signals across the phase-encoding steps are collected. Each signal is the spatial integral of the product between the unknown magnetizations and a spatial weighting modulated by the total magnetic field during one phase encoding step (Fig. 3, lower left panel). Subsequently, we solve a linear equation consisting of these signals and their associated spatial weightings (Fig. 3, lower right part) to reveal the spatial distribution of magnetization along each discretized frequency separately (the "*x*" step).

Specifically, the Fourier transform of $s(t,n)$ is

$$s(\omega,n)=\int_{\gamma|\mathbf{b}_{\text{readout}}(\mathbf{r})|=\omega}\rho(\mathbf{r})|\mathbf{e}_{m\perp}(\mathbf{r},n)|\exp\left(j\phi(\mathbf{r},n)\right)|\mathbf{c}_{\perp}(\mathbf{r})|J(\mathbf{r})dl, \quad [7]$$

Here, we describe the signal as the spatial integral of the magnetization with a particular precession frequency $\gamma|\mathbf{b}_{\text{readout}}(\mathbf{r})|=\omega$ spatially weighted by $|\mathbf{e}_{\text{m}\perp}(\mathbf{r},n)|\exp(j\phi(\mathbf{r},n))|\mathbf{c}_{\perp}(\mathbf{r})|J(\mathbf{r})$, where $J(\mathbf{r})=1/|\bigtriangledown(\gamma|\mathbf{b}_{\text{readout}}(\mathbf{r})|)|$ is the Jacobian corresponding to the changes between the spatial coordinate $\mathbf{r}$ and the frequency coordinate ω.

At each frequency ω, there are N phase-encoded measurements. Thus, Eq. [6] can be converted into a discrete linear equation $\mathbf{A\rho}=\mathbf{s}$. Each row of $\mathbf{A}$ is the associated spatial weighting $|\mathbf{e}_{\text{m}\perp}(\mathbf{r},n)|\exp(j\phi(\mathbf{r},n))|\mathbf{c}_{\perp}(\mathbf{r})|J(\mathbf{r})$ at a phase encoding step n. $\mathbf{s}$ is a vector of the measured complex-valued signal for frequency ω.

Conventional MRI, neglecting concomitant and remanence fields, typically uses N measurements to estimate the spatial distribution of the magnetization at N equally-spaced locations when the maximum, minimum, the increment, and the duration of the phase-encoding gradient satisfies the Nyquist theorem. Considering concomitant and remanence fields, in practice, it is still possible to estimate $\boldsymbol{\rho}$ at N equispaced locations (with respect to an orthogonal rectilinear Cartesian coordinate system) from N measurements. Yet, as demonstrated by the following simulations, we found that each iso-frequency curve in the image domain has to be discretized into N_{p}, $N_{\text{p}}\geq 2N$, equally-spaced locations in order to accurately capture the distribution of magnetization phase due to the inhomogeneous phase encoding caused by the concomitant and remanence fields. However, solving for $2N$ unknowns using N measurements is mathematically ill-posed. Thus, we propose to solve the underdetermined equation $\mathbf{A\rho}=\mathbf{s}$ by imposing a regularization constraint to minimize the ℓ_2-norm of $\mathbf{D\rho}$. $\mathbf{D}$ could be an identity matrix or a discrete difference operator taking the difference between neighboring pixels. The regularization using a discrete difference operator favors spatially smooth signals. Such a preference stems from the fact that typically N phase-encoding steps provide spatial weightings of the N lowest frequency modes. Therefore, by choosing a suitable regularization parameter λ, $\boldsymbol{\rho}$ can be estimated by minimizing the following cost function:

$$||\mathbf{A\rho}-\mathbf{s}||^2+\lambda\sigma\left(\mathbf{A}^{\text{H}}\mathbf{A}\right)||\mathbf{D\rho}||^2 \quad [8]$$

Here $\sigma(\mathbf{A}^{\text{H}}\mathbf{A})$ denotes the largest eigenvalue of $\mathbf{A}^{\text{H}}\mathbf{A}$. For the simulations and experiments in this paper with a well-behaving $\mathbf{A}$, we chose $\lambda<10$. Eq. [8] is solved repetitively for different ω to sweep over the precession frequencies determined by the FOV, the strength of the read-out gradient, and the duration of data acquisition. Finally, the reconstructed image $\boldsymbol{\rho}$ is interpolated over a two-dimensional or three-dimensional rectilinear image grid.

METHODS

Simulations

For the simulations, we calculated the magnetic fields generated by two gradient coils with the following field patterns: $(g_y z)\mathbf{e}_y+(g_y y)\mathbf{e}_z$ and $(-g_z x/2)\mathbf{e}_x+(-g_z y/2)\mathbf{e}_y+(g_z z)\mathbf{e}_z$. The coordinate origin was set at the center of the FOV. To solely focus on the concomitant field artifact, we set $\mathbf{c}(\mathbf{r})=(1,\ 0,\ 0)$ in the simulation. The concomitant fields were simulated by setting $\varepsilon=0$, 1, and 2, correspond to main field $B_0=\infty$, 64 and 32 μT with gradient strength 256 μT/m. A digital human brain phantom was constructed from a high-resolution three-dimensional T1-weighted structural MRI data set acquired at 3T (Tim Trio, Siemens Medical Solutions, Erlangen, Germany). The pulse sequence used to acquire this data was a standard MPRAGE (TR/TE/flip = 2530 ms/3.49 ms/7°, partition thickness = 1.0 mm, matrix = 256×256, 256 partitions, FOV = 256×256 mm^2). To accurately simulate the spatial integral describing the ULF-MRI signal (Eq. [2]), we simulated $s(t,n)$ using a two-dimensional spin-echo sequence with 128 phase encoding steps and 256 sampled time points by numerical integration over a two-dimensional spatial grid of 4096×4096 voxels. To approximate realistic measurements, Gaussian noise was added to the simulated signal such that the SNR, which was defined as the ratio between the standard deviation of the signal and the standard deviation of the noise, was 5.

To demonstrate the effectiveness of *f–x* reconstruction, we compare our method with previously proposed concomitant field correction algorithm. The first is the post-acquisition, pre-reconstruction correction algorithm proposed by Myers et al (20). We divided image domain into 32×32 regions and combine the corrected image in each region to form the final image. The second is the TDR method (21), we reconstruct the signal with 128×128 grid points and use properly chosen regularization parameter.

In addition, we used simulations to study the required number of discretization points N_{p} in order to accurately capture the distribution of magnetization phases due to concomitant and remanence fields described by Eq. [3]. Specifically, we reconstructed images with $N_{\text{p}}=N$ and $2N$ separately. We also studied the effect of the regularization parameter λ with values 10^{-5}, 10^{-3}, 10^{-1}, 10. We further studied the effect of the matrix $\mathbf{D}$ in Eq. [8] using

either an identity matrix or a difference operator taking the difference between image voxels to understand the effect on the reconstructed image.

Finally, the reconstructed images were linearly interpolated over 512×512 image voxels based on Delaunay triangulation using Matlab (Mathworks, Natick, MA).

Experiments

Experimental data were acquired with our customized system (5), which has a coil for magnetization precession $B_0 = 54.7$ μT, three gradient coils, an excitation coil, and a polarizing coil ($B_p = 24$ mT). The details of this prototype system are described in (5). The data were acquired from a spin-echo sequence in Figure 1. The readout length was 107 ms with a constant gradient strength $g_z = 85$ μT/m driven by a current of 2390 mA. Phase encoding was achieved by 58 steps with the maximal magnitude $g_x = 121$ μT/m and duration 38 ms with a 6-ms ramp time. The nominal resolution was 2.6×2.8 mm^2 and the corresponding strengths of the concomitant field effect in our experiment were $\varepsilon = 0.57$. The imaging time was 93 minutes including a 30-fold averaging.

Remanence Field and Concomitant Field Measurements

We first measured the *x*-, *y*-, and *z*-components of the remanence fields over the 100×82 mm^2 FOV by using a fluxgate magnetometer (MAG03-MC, Bartington Instruments Ltd., Oxford, England) positioned in a grid comprised of LEGO bricks (LEGO Systems, Billund, Denmark) resulting in a spatial resolution of 8×8 mm^2.

The sum of the gradient (*z*-directional component) and concomitant fields (*x*- and *y*-directional components) of the frequency and phase encoding coils were then measured separately using the same fluxgate magnetometer at steps of 16 mm. Since the remanence field was measured separately, the pure concomitant field pattern was derived empirically from the difference between these two measurements. To suppress noise, both frequency encoding and concomitant fields were linearly fitted and scaled according to the strengths used in the experimental sequence.

The *f*–*x* Formulation

To compare the computational efficiency, we simulated and reconstructed 15 square images of $n \times n$ pixels, where n was incremented from 8 to 120 in steps of 8 using our method and a direct time-domain reconstruction (TDR) algorithm (21). All images were reconstructed on the same computer (Quad-core CPU at 2.83 GHz, Intel, Santa Clara, CA; 8 Gbytes memory) using Matlab.

Given the empirically measured magnetic field data, we first separately interpolated the remanence field, concomitant field, phase- and frequency-encoding fields into the 0.1×0.1 mm^2 resolution using a cubic spline. The first "*f*" stage requires a map of iso-frequency curves of $\gamma |\mathbf{b}_{\text{readout}}(\mathbf{r})|$. Twenty-nine such curves ranging between 2211.9 Hz and 2472.1 Hz in steps of 9.29 Hz were constructed by identifying the nearest frequency over the field maps of 0.1×0.1 mm^2 resolution.

The second "*x*" stage requires $|\mathbf{e}_{m\perp}(\mathbf{r}, n)| \exp(j\phi(\mathbf{r}, n))| \mathbf{c}_\perp(\mathbf{r})| J(\mathbf{r})$ on 334 discretization points along each iso-frequency curve. The spatial distributions of $|\mathbf{e}_{m\perp}(\mathbf{r}, n)|$ at each step of the phase encoding were derived from $\mathbf{b}_{\text{readout}}(\mathbf{r})$ and the magnetization at the beginning of the readout after the nth phase encoding based on the waveforms of the phase-encoding step and the estimated concomitant and remanence fields. In theory, we need a map of the coil sensitivity $\mathbf{c}(\mathbf{r})$ to calculate $\phi(\mathbf{r},n)$. However, without knowing the actual $\mathbf{c}(\mathbf{r})$, we only estimated the incremental phase $\Delta\phi(\mathbf{r},n)$ in each phase-encoding step: $\phi(\mathbf{r},n) = \phi_0(\mathbf{r}) + \Delta\phi(\mathbf{r},n)$. In practice, $\Delta\phi(\mathbf{r},n)$ was estimated from the angle between $\mathbf{e}_{m\perp}(\mathbf{r}, n)$ and $\mathbf{e}_{m\perp}(\mathbf{r}, n = n_{PE})$, where n_{PE} represents the phase-encoding step without any current in the phase-encoding coil.

Taken together, without further information on coil sensitivity $\mathbf{c}(\mathbf{r})$, in this study, we only reconstructed an image of $\rho(\mathbf{r}) \exp(j\phi_0(\mathbf{r}))|\mathbf{c}_\perp(\mathbf{r})|$. Finally, we linearly interpolated the reconstructed magnetization distributed along N_p discretization points on each iso-frequency curve into 274×334 image voxels using Delaunay triangulation by Matlab.

RESULTS

Computational Time and Complexity

We first studied the computational complexity of our proposed method compared to conventional 2D fast Fourier transform algorithm and direct time-domain method (21). For an image of *m*-by-*n* pixels (thus spatially encoded by n phase-encoding steps and m frequency-encoded samples), the fast Fourier transform algorithm with the complexity of $O(m \log m)$ has to be repeated n times (across n phase encoding steps) in the first "*f*" stage. This accounts for the complexity of $O(n\, m \log m)$. Subsequently, we need to solve m sets (across different iso-frequency curves) of n linear equations, each set of which amounts to the complexity of $O(n^3)$. The second "*x*" stage thus has the complexity of $O(m\, n^3)$. Taken together, since the latter "*x*" stage dominates the computational load, the total complexity of our method is $O(m\, n^3)$, which is much improved compared to the TDR method with computational complexity of $O(m^3\, n^3)$. Figure 4 shows the empirical computational time for different image matrix sizes. We extrapolated the computation time required for larger image matrices by linearly fitting the computation time for data with $n \geq 48$. The ratio between slopes using TDR and the *f*–*x* method was 1.6, which approximates to the $O(n^2)$ difference (ratio between slopes = 1.5) between the two methods. This clearly shows the computational efficiency of the *f*–*x* hybrid method, especially at a large image matrix size.

Figure 5A–D shows the reconstructed simulation images of the human brain phantom including the remanence field and the concomitant field with $\varepsilon = 0$, 1, and 2 using Fourier transform, post-acquisition pre-reconstruction method (20), TDR method, and the *f*–*x* hybrid method with $N_p = 256$, $\mathbf{D}$ as a difference operator and $\lambda = 10^{-2}$ (see Eq. [8]). At $\varepsilon = 1$, the Fourier-reconstructed image shows compressed frontal lobes and inflated occipital lobes along the left-right direction due to the concomitant fields (Fig. 5E). Such artifacts become even

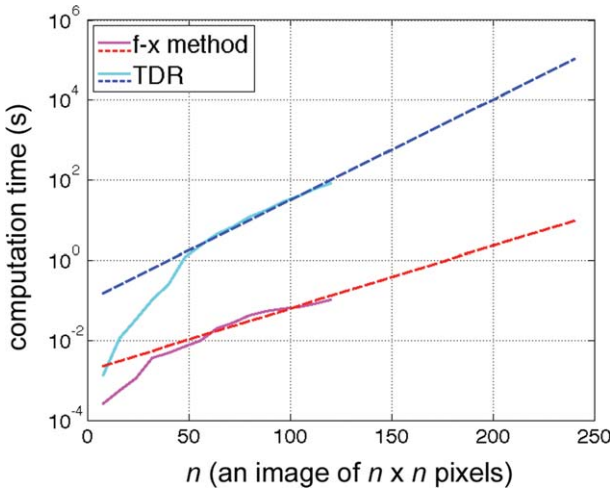

FIG. 4. The fitted (dashed lines) and the empirical (solid lines) computational time for an image of $n \times n$ pixels using TDR (blue and cyan colors) and the *f–x* method (red and magenta colors).

stronger at $\varepsilon = 2$. The post-acquisition pre-reconstruction method reconstructed images without much distortion and blurring despite a little intensity drop at the lower part of the image at $\varepsilon = 1$. This artifact became more seriously at $\varepsilon = 2$ (Fig. 5B). The TDR method reconstructed the image without distortion or blurring at $\varepsilon = 1$. At $\varepsilon = 2$, even without noise, we observe that lower part of the image became noisy. This is due to the fact that the rectangular grid used in the TDR method could not approximate the signal equations well when the encoded spatial frequencies are higher than expected. The *f–x* hybrid method can reconstruct the image without much distortion. However at $\varepsilon = 2$, prominent residuals were evident in the lower left and right corners. This is likely due to aliasing. Note that the noise distribution is spatially inhomogeneous, most likely because of the spatially varying conditioning of the encoding matrix **A** in Eq. [8] across the different iso-frequency curves. Images with a stronger concomitant field ($\varepsilon = 2$) show a higher noise level than in the case $\varepsilon = 1$. Including the simulated remanence field (Fig. 5E) further distorted the image by compressing the right frontal lobe in the anterior-posterior direction. Still, the *f-x* hybrid method reconstructed the image without visible distortion, except that the aliasing artifacts appear at the lower left and right corners.

Figure 6 shows the simulated reconstructions using different numbers of discretization points N_p in evaluating

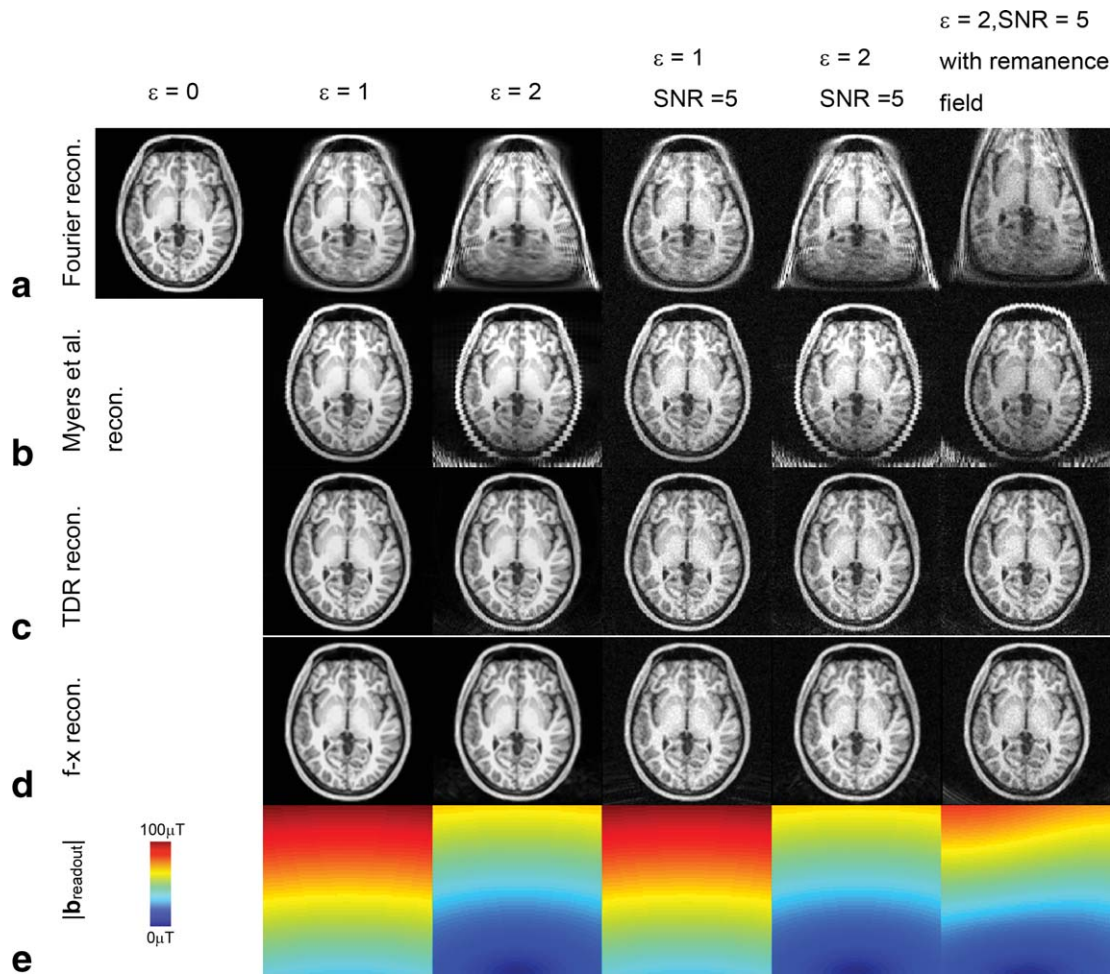

FIG. 5. Brain-phantom images reconstructed using Fourier transform (**a**), method proposed by Myers et al. (**b**), TDR method (**c**), and the *f–x* method (**d**). The spatial distribution of the magnetic field during readout $|\mathbf{b}_{readout}(\mathbf{r})|$ (**e**) with concomitant fields ($\varepsilon = 1$ and $\varepsilon = 2$), the remanence field, and contaminating noise.

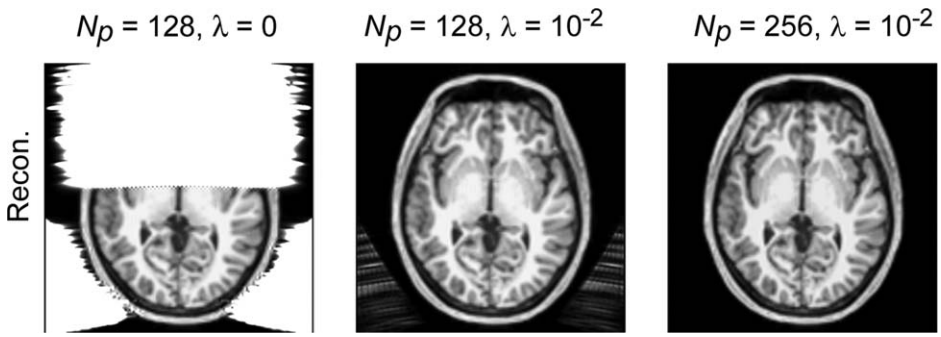

FIG. 6. The reconstructed images using the *f–x* method with a different number of discretization points N_p with and without regularization with concomitant fields $\varepsilon = 1$.

Eq. [7] with a concomitant field strength of $\varepsilon = 1$. We can see that when $N_p = N$ without any regularization, the reconstructed image shows serious artifacts because (1) the discretization in Eq. [7] fails to represent the integration accurately, and (2) the encoding matrix **A** in Eq. [8] is extremely ill-conditioned. Adding a regularization term can mitigate the artifact arising from the latter reason. Still, at locations with a strong concomitant field (right and left lower corners), we cannot describe the integration accurately using $N_p = N$. When N_p is increased to $2N$, the image can be reconstructed with minimally visible residuals. Thus, all the following reconstructions in this work use $N_p = 2N$. Even higher N might be necessary in the case of stronger distorting fields.

Figure 7 shows simulated reconstructions using different regularization parameters with SNR = 5. With λ between 10^{-1} and 10^{-3} the quality of the reconstructions were similar, while less regularization ($\lambda = 10^{-3}$) resulted in an amplified background noise. This is reasonable, since a strong regularization parameter yields spatially smoother and thus less noisy images. Using $\lambda = 10$ overly emphasized the prior information and thus the reconstructed image was blurred. When the regularization parameter was too small ($\lambda = 10^{-5}$), the conditioning of the encoding matrix **A** in Eq. [8] became unstable and the reconstructed image shows significantly amplified noise. Generally, λ ranging between 10^{-1} and 10^{-3} gave a stable reconstruction.

Figure 8 shows simulated reconstruction with $\lambda = 10^{-2}$ using either an identity matrix or a difference operator taking the difference between neighboring pixels as the matrix **D** in Eq. [8]. Little difference between the reconstructions was found, except that the background noise at the lower left and right corners was slightly amplified when the difference operator was used for **D**. This result suggests that the two choices for **D** only marginally modulate the reconstruction with the chosen regularization parameter.

The spatial distribution of the remanence field $\mathbf{b}_{rem}$ and the strength of the total field with and without the remanence field $\mathbf{b}_{rem}$ are shown in Figure 9. The remanence field was found to be rather inhomogeneous for all magnetic field components. The magnitude of the remanence field was within ± 3 μT. The strength of the total field was maximally about 60 μT, much larger than the strength of the remanence field. However, the gradient of $\mathbf{b}_{rem}$ is locally strong, which causes distortion of the iso-frequency lines.

Figure 10 shows the reconstructed images from five channels of the ULF-MRI system using the *f–x* method. The total computation time was less than 2 s. These five channels were closest to the grid phantom and they had the highest SNR. We reconstructed the image in two ways: using either only the *z*-component of $\mathbf{b}_{rem}$ and using both $\mathbf{b}_{rem}$ and $\mathbf{b}_{con}$. This was done to compare our method to the distortion correction methods in high-field MRI with a field map. Figure 8 also shows the sum-of-squares (SoS) image. Compared with the photo of the phantom, we found that the image reconstructed by the Fourier transform readily shows prominent distortions structure.

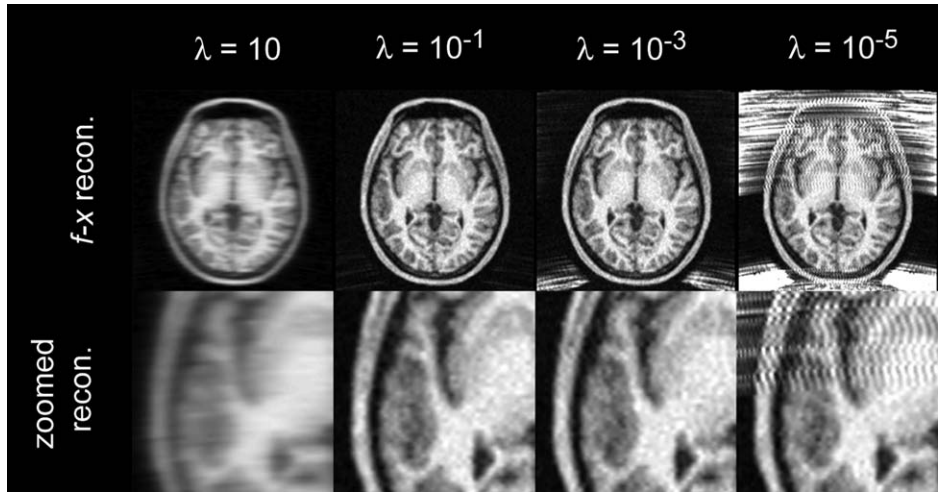

FIG. 7. The images reconstructed by the *f–x* method using different regularization parameters (upper row) with concomitant fields $\varepsilon = 1$ and the magnified image around the left temporal lobe (lower row).

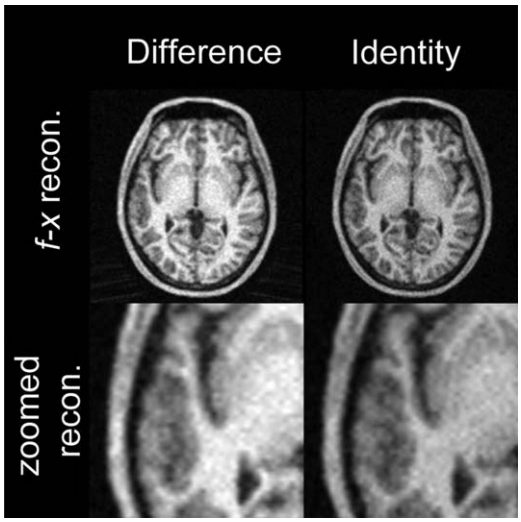

FIG. 8. The images reconstructed by the *f–x* method using either a linear operator taking the difference between neighboring image voxels or an identity matrix in the regularization matrix with concomitant fields $\varepsilon = 1$. The lower row shows magnified images around the left temporal lobe.

Specifically, the grid was dilated at the left side and compressed at the right side of the image. With only the effect of *z*-component of $\mathbf{b}_{\mathrm{rem}}$ corrected, the distortion was reduced but still noticeable. Provided with the complete $\mathbf{b}_{\mathrm{rem}}$ and $\mathbf{b}_{\mathrm{con}}$, the *f–x* hybrid method corrected this distortion significantly.

DISCUSSION

This study presents a computationally efficient method of reconstructing ultra-low-field MR images with reduced distortion caused by the concomitant and remanence fields. With validations of the methods largely done through simulations, we demonstrated that this method is capable of correcting distortions even with strong concomitant field artifacts ($\varepsilon = 2$; Fig. 5), because our method describes the magnetization dynamics considering all the effects due to the remanence and concomitant fields of three spatial components. This method is computationally efficient as it uses a combination of the fast Fourier transform algorithm and a linear equation solver (Fig. 4). With sufficiently dense discretization in solving the linear equation (Fig. 6), the performance of this *f–x* method was found to be stable with different choices of the regularization parameter (Fig. 7) and the regularization matrix (Fig. 8). Empirical data demonstrated that visible distortion was corrected efficiently (Fig. 10).

When the concomitant field effect is moderate ($\varepsilon \leq 1$) (20), the artifact can be corrected by image post-processing using the Fourier reconstruction method after respectively correcting the local magnetization phases and frequencies disturbed by the concomitant fields in phase- and frequency-encoding directions. Stronger concomitant field artifacts can be corrected by the TDR method, which directly relates the detected MRI signal to magnetization dynamics under the influence of a stronger concomitant field (21). However, the signal equation in the TDR can be too large to be solved (see our computational complexity analysis). Another limitation of the TDR method is that due its limited computational efficiency, the spatial integration (Eq. [6]) is typically evaluated over $n_{\mathrm{p}} \times n_{\mathrm{f}}$ equidistant discretized spatial locations, where n_{p} and n_{f} are the number of phase and frequency encoding steps respectively. However, such an equidistant spatial grid may not be able to capture the magnetization dynamics accurately considering the disturbance from concomitant and remanence fields.

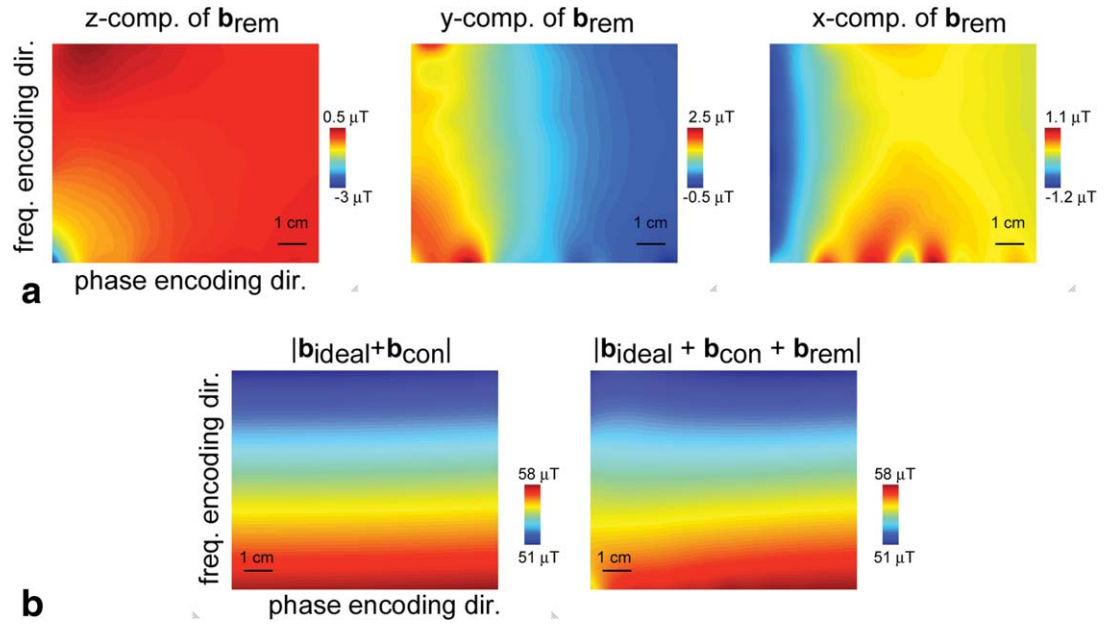

FIG. 9. **a:** The spatial distribution of the *x*-, *y*-, and *z*-component of the remanence field. **b:** The spatial distribution of the strength of the concomitant field and the strength of the sum of the concomitant and remanence fields.

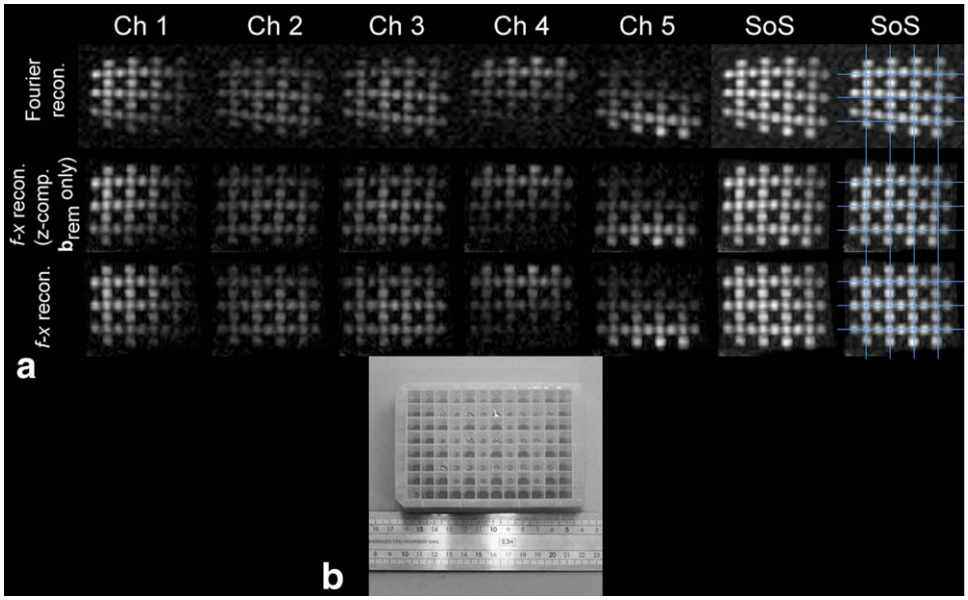

FIG. 10. **a:** The reconstructed images of five channels of the ULF-MRI system and the sum-of-squares (SoS) image using the Fourier transform, *f–x* method using only the *z*-component of the remanence field and the *f–x* method using both the remanence and concomitant fields. The added blue grid may facilitate observing the distortion. **b:** A photo of the phantom.

Our method can reconstruct MRI signals affected by a strong concomitant field ($\varepsilon > 1$; Fig. 5). Similar to TDR, our method also describes magnetization dynamics in signal generation. However, we use the Fourier transform in the frequency-encoding direction and thus it is computationally more efficient. Furthermore, based on the spatial distribution of iso-frequency curves derived from the total magnetic field (including concomitant and remanence fields), our method can directly reveal the spatial distribution of magnetization precessing at different frequencies. This avoids the necessity of evaluating the signal integration (Eq. [6]) in the frequency-encoding direction over equidistant discretized spatial locations as required in TDR. Along the phase-encoding direction, we mitigate the risk of inaccurate signal integration over equidistant spatial locations by using a two times denser equidistant spatial locations than what is required for TDR.

High-precision measurement of the total magnetic field is crucial in a successful image reconstruction using TDR or the *f–x* method. This is because TDR requires knowledge of the direction of the magnetization over the FOV. The *f–x* method also requires the knowledge of $|\mathbf{e}_{m\perp}|$. Such information is only available when the local oscillator and analog-to-digital converter have high temporal accuracy and the gradient coils generate high-SNR magnetic fields. However, here ε was approximately 0.6. When also considering the remanence field, our experimental data had $|\mathbf{e}_{m\perp}| > 0.99$. In this case, we used $|\mathbf{e}_{m\perp}| = 1$ in the reconstruction.

Most distortion correction methods, including those applied to high-field MRI, require some calibration information, such as a field map. Our method also needs such calibration information: the spatial distribution of concomitant and remanence fields. Fortunately, such information needs only to be measured once and it can be applied to all subsequent measurements, when the following conditions are met: (1) the concomitant fields, including all directional components, are accurately measured with precise spatial localization, (2) the concomitant fields are linearly scaled with the current driving the gradient, (3) the total concomitant fields generated by all gradient coils are the summation of the concomitant fields generated by each gradient coil, (4) the gradient system is stable over time, and (5) the coregistration between measured concomitant fields and the imaging area is accurate such that imaging FOV can be accurately derived within the FOV used for concomitant field measurements. Ensuring the validity of these five assumptions are clearly the foundation of using the *f–x* method to reduce ULF MRI distortions.

The concomitant fields can be derived from imaging gradient, if the geometry of the gradient coils and the driving current are known accurately. However, in practice, it is more convenient to measure the concomitant fields directly.

It is well known that both concomitant and remanence fields can have a through-plane effect. Because of the structure of our phantom, we only show images over one plane with clearly reduced in-plane distortion. Therefore people may speculate that the *f–x* method is only useful in multi-slice imaging. However, it is important to note that, due to the limitation of gradient strength, volumetric ULF MRI is typically achieved by partition encoding rather than by multiple slice-selection. Our method may be able to correct through-plane distortion when concomitant and remanence fields distribution over a volume is available. However, this hypothesis requires further experimental evidence to support it. We will work on this as the future development of the *f–x* method.

Our method can reduce the artifacts due to the concomitant and remanence fields; however, the reconstructed image is not perfect (Figs. 5 and 10). This may be explained by two potential reasons: first, the local resolution along the frequency-encoding direction is determined by the magnitude of the gradient of the magnetic field during the frequency encoding. Considering the total field generated by the frequency-encoding magnetic

field, concomitant field, and remanence field, it is possible that the magnitude of the total magnetic field during frequency encoding at some locations in the FOV is rather smooth. Thus, the spatial resolution becomes rather inhomogeneous over the FOV. Second, the concomitant and remanence fields can disturb the desired incremental phase-encoding gradient moments required for spatial encoding. Aliasing-like and blurring artifacts can respectively occur at locations with a stronger or weaker magnetic field than required in the ideal phase encoding.

Based on Eq. [2], the situation of multiple frequency surfaces and spatial aliasing occurs when the gradient field is so strong that the $\varepsilon > 2$. In such a situation, our method using only a single receiver coil cannot reconstruct an image unambiguously. However, it is conceivable that when there are multiple receivers with distinct sensitivities, our method may be able to resolve this difficulty.

This *f*–*x* method is similar to the method of reconstructing high-field MRI encoded by nonlinear spatially encoded magnetic fields (SEMs) (23). In this high-field acquisition, both phase and frequency encodings still work reasonably well such that two-dimensional Fourier transform can be applied to generate an image over a non-Cartesian coordinate system. Subsequent interpolation is needed to restore the image over the Cartesian coordinate system. However, when disturbed by concomitant and remanence fields, we cannot apply the Fourier transform along the phase-encoding direction, because the incremental gradient moment for each phase-encoding step is no longer constant. Thus we have to solve a set of linear equations (Eq. [8]) instead of using the Fourier transform.

While there are numerous methods (24,25) for correcting distortion artifacts in high-field MRI, the principal difference is that these methods only account for the field disturbance along the main magnetic field direction. Magnetization is still considered precessing only around the z axis during phase and frequency encoding. Differently, in ULF MRI, magnetization can precess around any direction of the axis during phase and frequency encoding. Figure 10 clearly demonstrates this difference: when only considering the disturbance on magnetization precession over a constant plane like in high-field MRI, the reconstruction still shows prominent distortion.

The *f*–*x* method is indeed a distortion correction on top of the Fourier transform. Importantly, the "Fourier transform" in this context incorporates all physical disturbances generated by concomitant and remanence fields in order to generate a correct spatial distribution of magnetization. Our method is certainly not the traditional fast Fourier transform (FFT) method and thus it takes longer time than applying the FFT along both phase and frequency encoding axes. To our understanding, there is no method of correcting distortion in ULF MRI generated by fields in both phase and frequency axes *after* sum-of-squares image reconstruction. Our method is one approach aiming at mitigating this technical challenge by integrating the Fourier transform and distortion correct in the phase encoding direction in one step.

The proposed method is not only limited to the spin echo pulse sequence, for example we can achieve phase encoding by modulation the duration of the phase-encoding gradient with fixed amplitude. Although the accrued phase is linearly increased in different phase encoding steps when using a phase encoding gradient with a fixed amplitude and linearly-stepped durations, two issues different from the conventional MRI prevent us from using the Fourier transform to obtain distortion-free spatial information directly. First, because of concomitant fields, the magnetization at the beginning of phase encoding may not be orthogonal to the magnetic field. This means that only the orthogonal component of magnetization with respect to the magnetic field will be encoded among phase encoding steps, while the magnetization component in parallel to the magnetic field cannot be encoded. This parallel magnetization component will appear as signal at zero frequency after Fourier transform along the phase encoding direction. The second issue is, because of concomitant fields, the magnetization precession axis in phase encoding is not in parallel with the magnetization precession axis in frequency encoding. In an exemplary problematic case, suppose at one particular location where these two precession axes are perpendicular to each other and the magnetization aligns with the frequency encoding magnetic field after phase encoding. Since the magnetization has no perpendicular component with respect to the frequency encoding field, we can no longer detect such DC signal originating from that particular location. However, the above-mentioned two challenges can be mitigated by our method, because these physical phenomena have explicitly modeled in the encoding matrix (Eq. [7]).

Although we did not demonstrate our method to achieve spatiotemporal resolution enhancement or the optimal combination across channels using the SENSE method (26), we expect that these can be achieved if the sensitivity information is available in Eq. [7]. In ULF MRI, the SNR is typically too low to be traded-off for spatiotemporal resolution enhancement. We also expect that our method can be used to reconstruct images using data collected using any k-space trajectory, in which the magnetic field during the read-out is constant. This includes rectilinear Cartesian k-space sampling and a radial *k*-space trajectory. Further studies are required to demonstrate the feasibility of our method in such generalized cases.

REFERENCES

1. Clarke J, Hatridge M, Mößle M. SQUID-detected magnetic resonance imaging in microtesla fields. Ann Rev Biomed Eng 2007;9:389–413.
2. Packard M, Varian R. Free nuclear induction in the earths magnetic field. Phys Rev 1954;93:941–941.
3. Fischer HW, Rinck PA, Vanhaverbeke Y, Muller RN. Nuclear-relaxation of human brain gray and white matter - analysis of field-dependence and implications for MRI. Magnet Reson Med 1990;16: 317–334.
4. Busch S, Hatridge M, Mößle M, Myers W, Wong T, Mück M, Chew K, Kuchinsky K, Simko J, Clarke J. Measurements of T_1-relaxation in ex vivo prostate tissue at 132 μT. Magn Reson Med 2012;67: 1138–1145.
5. Vesanen PT, Nieminen JO, Zevenhoven KC, et al. Hybrid ultra-low-field MRI and MEG system based on a commercial whole-head neuromagnetometer. Magn Reson Med 2013;69:1795–1804

6. Norris DG, Hutchison JMS. Concomitant magnetic-field gradients and their effects on imaging at low magnetic-field strengths. Magn Reson Imaging 1990;8:33–37.
7. Volegov PL, Mosher JC, Espy MA, Kraus RH Jr. On concomitant gradients in low-field MRI. J Magn Reson 2005;175:103–113.
8. Yablonskiy DA, Sukstanskii AL, Ackerman JJH. Image artifacts in very low magnetic field MRI: The role of concomitant gradients. J Magn Reson 2005;174:279–286.
9. Bernstein MA, Zhou XJ, Polzin JA, King KF, Ganin A, Pelc NJ, Glover GH. Concomitant gradient terms in phase contrast MR: analysis and correction. Magn Reson Med 1998;39:300–308.
10. Zhou XJ, Du YP, Bernstein MA, Reynolds HG, Maier JK, Polzin JA. Concomitant magnetic-field-induced artifacts in axial echo planar imaging. Magn Reson Med 1998;39:596–605.
11. Du YP, Joe Zhou X, Bernstein MA. Correction of concomitant magnetic field-induced image artifacts in nonaxial echo-planar imaging. Magn Reson Med 2002;48:509–515.
12. King KF, Ganin A, Zhou XJ, Bernstein MA. Concomitant gradient field effects in spiral scans. Magn Reson Med 1999;41:103–112.
13. Sica CT, Meyer CH. Concomitant gradient field effects in balanced steady-state free precession. Magn Reson Med 2007;57:721–730.
14. Zhou XJ, Tan SG, Bernstein MA. Artifacts induced by concomitant magnetic field in fast spin-echo imaging. Magn Reson Med 1998; 40:582–591.
15. Meriles CA, Sakellariou D, Trabesinger AH, Demas V, Pines A. Zero- to low-field MRI with averaging of concomitant gradient fields. Proc Natl Acad Sci USA 2005;102:1840–1842.
16. Meriles CA, Sakellariou D, Trabesinger AH. Theory of MRI in the presence of zero to low magnetic fields and tensor imaging field gradients. J Magn Reson 2006;182:106–114.
17. Bouchard L-S. Unidirectional magnetic-field gradients and geometric-phase errors during Fourier encoding using orthogonal ac fields. Phys Rev B 2006;74:054103.
18. Kelso N, Lee S-K, Bouchard L-S, Demas V, Mück M, Pines A, Clarke J. Distortion-free magnetic resonance imaging in the zero-field limit. J Magn Reson 2009;200:285–290.
19. Zotev VS, Volegov PL, Matlashov AN, Espy MA, Mosher JC, Kraus RH. Parallel MRI at microtesla fields. J Magn Reson 2008;192: 197–208.
20. Myers WR, Mossle M, Clarke J. Correction of concomitant gradient artifacts in experimental microtesla MRI. J Magn Reson 2005;177: 274–284.
21. Nieminen JO, Ilmoniemi RJ. Solving the problem of concomitant gradients in ultra-low-field MRI. J Magn Reson 2010;207:213–219.
22. Magnelind PE, Gomez JJ, Matlashov AN, Owens T, Sandin JH, Volegov PL, Espy MA. Co-registration of interleaved MEG and ULF MRI using a 7 channel low-T_c SQUID system. IEEE Trans Appl Supercond 2011;21:456–460.
23. Schultz G, Ullmann P, Lehr H, Welz AM, Hennig J, Zaitsev M. Reconstruction of MRI data encoded with arbitrarily shaped, curvilinear, nonbijective magnetic fields. Magn Reson Med 2010;64: 1390–1404.
24. Doran SJ, Charles-Edwards L, Reinsberg SA, Leach MO. A complete distortion correction for MR images: I. Gradient warp correction. Phys Med Biol 2005;50:1343–1361.
25. O'Donnell M, Edelstein WA. NMR imaging in the presence of magnetic field inhomogeneities and gradient field nonlinearities. Med Phys 1985;12:20–26.
26. Pruessmann KP, Weiger M, Scheidegger MB, Boesiger P. SENSE: sensitivity encoding for fast MRI. Magn Reson Med 1999;42:952–962.